Acta Astronautica 174 (2020) 254–269

Contents lists available at ScienceDirect

Acta Astronautica

journal homepage: www.elsevier.com/locate/actaastro

Wall heat transfer prediction in CH_4/O_2 and H_2/O_2 rocket thrust chambers using a non-adiabatic flamelet model

Nikolaos Perakis*, Oskar J. Haidn

Chair of Space Propulsion, Technical University of Munich, Boltzmannstr. 15, 85748, Garching, DE, Germany

ARTICLE INFO

Keywords:
Rocket engines
Methane combustion
Wall heat transfer
Recombination reactions
Flamelet modelling

ABSTRACT

The current work presents the extension of the flamelet model for turbulent combustion calculations to account for deviations from adiabatic conditions. The aforementioned extension is expected to significantly improve the prediction of the chemical processes occurring in the vicinity of cooled walls in rocket engine applications. A lower enthalpy level leads to an increase of the recombination reactions, which is of particular interest in the case of methane/oxygen combustion. In the present approach, the flamelet equations are solved in mixture fraction space and the energy equation is replaced by a prescription of the enthalpy profile in order to include non-adiabatic effects. To avoid the over-prediction of the recombination reactions, a local "freezing" of the chemical reactions is introduced based on the Damkoehler number close to the cold wall boundary. A pre-tabulation of the chemical time-scales in the flamelet tables enables a fast calculation of the Damkoehler number. The model is verified both for CH_4/O_2 and H_2/O_2 using the simulation of a cooled reacting boundary layer. The extended hybrid model is employed for the simulation of a single-element rocket thrust chamber using CH_2/O_2 and H_2/O_2 and is compared to the non-adiabatic and frozen flamelet models. A more accurate wall heat transfer and pressure level prediction is achieved with the hybrid model for both propellant combinations leading to great agreement with the available experimental measurements.

1. Introduction

Turbulent combustion processes are present in a large number of engineering problems. Of particular interest are the applications, which include flame-wall interaction and convective heat losses. Wall-confined reacting flows subject to heat losses to the wall are always found in gas turbine combustion chambers and rocket engine thrust chambers. In both cases, the interaction of the hot gas and the wall leads to heat loads that must be taken into account in the design process of the engine.

The proper design of the cooling system is especially crucial in the case of rocket engines. The high velocity flows with adiabatic temperature exceeding 3500 K within the thrust chamber can lead to extreme heat flux values of up to 150 MW/m_2 in the nozzle due to the steep temperature gradients [1]. Moreover, the tendency in liquid rocket engines is to use high operating pressures in order to achieve higher specific impulse, compactness of the chamber and a higher nozzle expansion ratio for a given exhaust diameter [2]. Increasing the chamber pressure however, has a direct impact on the wall heat loads, since the heat transfer coefficient is approximately linearly proportional to the chamber pressure: $\dot{q} \sim p^{0.8}$ [3]. An insufficient cooling of the structure would rapidly lead to a mechanical damage of the flight hardware and a mission failure. Therefore, the design of thrust chambers has to meet many conflicting requirements simultaneously such as high performance, reliable cooling, low weight, structural safety and costs.

Measurements of the wall heat loads with experimental methods in the design process of a rocket engine can be done with high-cost firing tests. In order to reduce the development costs of new rocket engines, expensive trial-and-error has to be kept at a minimum. For that reason, numerical methods for the accurate description of the combustion and heat transfer processes are necessary. At the same time however, the computational cost of these methods should not be too high, in order to allow for fast estimations of the performance and the heat loads in the early design process of the components and systems. The simulation of turbulent combustion within rocket engines usually needs the incorporation of detailed chemistry. In engineering applications using RANS, the Finite Rate Model and the Eddy Dissipation Concept are often utilized to account for the chemical reactions between the species. These detailed models however require the solution of $N_{sp} - 1$ additional equations for the N_{sp} species being modeled. Moreover, accounting for the Turbulence Chemistry Interaction (TCI) in those

* Corresponding author.
E-mail addresses: nikolaos.perakis@tum.de (N. Perakis).

https://doi.org/10.1016/j.actaastro.2020.05.008
Received 26 April 2020; Received in revised form 30 April 2020; Accepted 5 May 2020
Available online 12 May 2020

Nomenclature

c_p	specific heat capacity [J/(kg·K)]
Da	Damkoehler number [−]
h	specific enthalpy [J/kg]
J	Jacobi matrix [1/s]
k	turbulence kinetic energy [m²/s²]
M	molecular weight [kg/mol]
$\dot{m}$	mass production rate [kg/(m³·s)]
N	upper limit index [−]
P	Probability Density Function PDF [−]
p	pressure [bar]
Pr	Prandtl number [−]
$\dot{Q}$	heat rate [W]
$\dot{q}$	heat flux [W/m²]
R	universal gas constant [J/(kg·K)]
r	grid refinement ratio [−]
Sc	Schmidt number [−]
T	temperature [K]
t	time [s]
u	velocity [m/s]
x, y	spatial coordinates [m]
Y	species mass fractions [−]
Z	mixture fraction [−]
Z''^2	mixture fraction variance [−]
ε	turbulence dissipation rate [m²/s³]
ε	numerical error [−]
ζ	normalized enthalpy [−]
λ	thermal conductivity [W/(m·K)]
μ	viscosity [Pa·s]
ρ	density [kg/m³]
τ	time-scale [s]
φ	generic variable [−]
χ	scalar dissipation rate [−]
ψ	apparent numerical order [−]
$\dot{\omega}$	reaction rate [1/s]

Subscripts

ad	adiabatic
chem	chemical
ex	extinction
ext	exact
flow	flow
fu	fuel
k	species index
min/max	minimum/maximum
n	normalized
ox	oxidizer
sp	species
st	stoichiometric value
tar	target value
t	turbulent value
wall	quantity at the wall

Abbreviations

FRC	Finite Rate Chemistry
FRF	Frozen Flamelet
HYF	Hybrid Flamelet
GCI	Grid Convergence Index
NAF	Non-adiabatic Flamelet
PDF	Probability Density Function
RANS	Reynolds Averaged Navier Stokes
TCI	Turbulence-Chemistry Interaction

models requires a closure using probability density functions (PDFs), which is complex due to the large number of transported variables requiring either multi-dimensional assumed PDFs [4] or very expensive transported PDF methods [5].

For that reason, efforts have been made in order to reduce the complexity of the turbulent combustion simulations by introducing simplified models with a smaller number of equations, which directly accelerates the computation. A common method used for the simulation of H_2/O_2 rocket engines is the assumption of chemical equilibrium and is justified by the high pressure and high temperature combustion environment as well as by the fast time-scales of the hydrogen combustion.

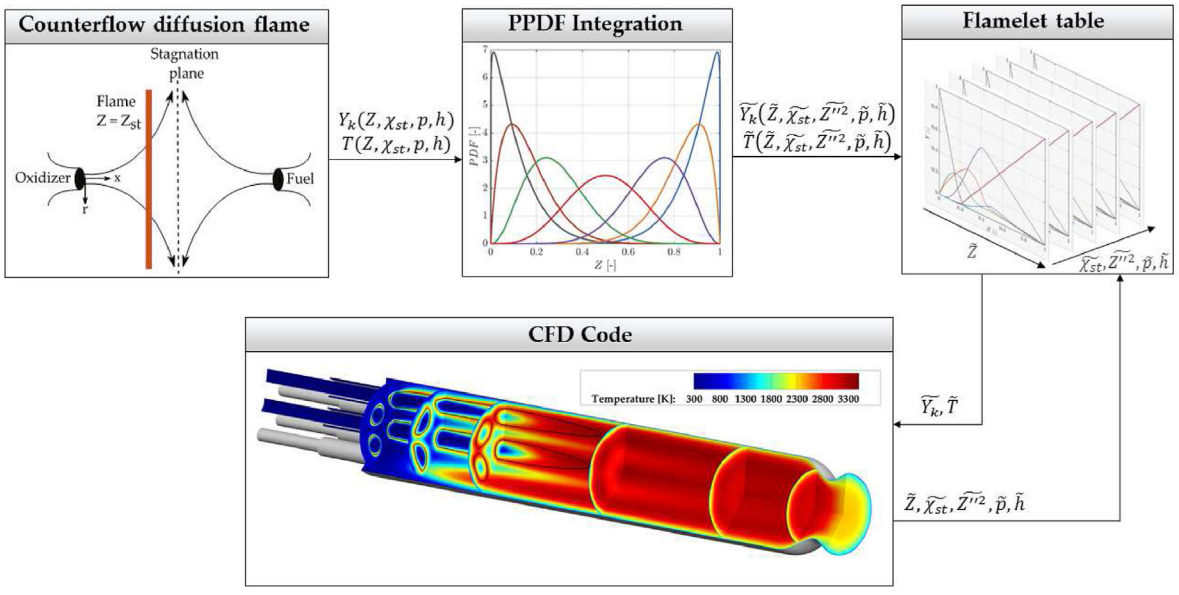

Fig. 1. Schematic illustration of the flamelet table generation and coupling with the computational fluid dynamics (CFD) solver.

In the case of hydrocarbon combustion such as CH_4/O_2 however, the assumption of chemical equilibrium is no longer valid. The increased complexity of the chemical mechanism, combined with the slow time-scales of chemical kinetics give rise to non-equilibrium effects. In order to overcome this insufficiency of the equilibrium model, the flamelet model has been widely used in many rocket engine simulations using CH_4/O_2 as propellants. The classical steady flamelet model [6], is able to capture the departure from the chemical equilibrium, but needs to be extended in order to account for changes in the gas composition in the presence of low-enthalpy regimes, as is the case in cooled rocket engine walls. In the present study, an extension of the flamelet model is undertaken, in order to capture non-adiabatic effects in the presence of wall heat losses.

2. Flamelet combustion model

In many practical engineering applications, including rocket thrust chambers, the equilibrium model has been applied in order to describe the occurring chemical processes. For the description of propellants with complex chemistry and large time-scales however, the flamelet model has been widely implemented, since it is able to capture non-equilibrium effects.

According to the flamelet turbulent combustion model, the turbulent flames are viewed as an ensemble of local flame structures with laminar nature (laminar flamelets), which are affected by the turbulent flow by being stretched and wrinkled. This assumption is valid when the relevant chemical scale is short compared to the convection and diffusion time scales, since under those conditions combustion takes place within the asymptotically thin flamelets, embedded in the turbulent flow [7].

This enables the decoupling of the chemical and turbulent processes and hence a significant reduction in computational time, while still allowing for the use of a detailed chemical reaction mechanism. The calculation of the laminar flamelets is carried out in a pre-processing step, while the presence of turbulent fluctuations is accounted for by a Presumed Probability Density Function (PPDF) [8]. The thermo-chemical data of the turbulent flamelet solutions can then be tabulated as a function of a reduced set of scalars, which results in significant speed-up of the simulation. This concludes the pre-processing step as illustrated in Fig. 1.

2.1. Laminar flamelets

The calculation of the one-dimensional local laminar flame structures (i.e. laminar flamelets) takes place by solving multiple instances of the counterflow diffusion flame problem. The solution of the 1D problem can be done either in the physical or in the mixture-fraction space. In mixture fraction space, the simplified set of the flamelet equations consists of the governing equations for the chemical species and the temperature (or enthalpy) of the one-dimensional flame structure. In this coordinate frame, only the gradients perpendicular to the iso-surface of the mixture fraction are dominant and all gradients on the iso-surface can be neglected [8]. The resulting equations are given as follows under the assumption of unity Lewis number for all chemical species [7].

$$\frac{\partial Y_k}{\partial t} = \frac{1}{2}\chi\frac{\partial^2 Y_k}{\partial Z^2} + \frac{\dot{m}_k}{\rho} \tag{1}$$

$$\frac{\partial T}{\partial t} = \frac{1}{2}\chi\frac{\partial^2 T}{\partial Z^2} - \frac{1}{\rho c_p}\sum_{k=1}^{N_{sp}} h_k \dot{m}_k + \frac{1}{2c_p}\chi\left[\frac{\partial c_p}{\partial Z} + \sum_{k=1}^{N_{sp}} c_{p,k}\frac{\partial Y_k}{\partial Z}\right]\frac{\partial T}{\partial Z} \tag{2}$$

where Y_k, $\dot{m}_k$and h_k denote the mass fraction, mass production rate and specific enthalpy of species k respectively, while Z, T, ρ, c_p stand for the mixture fraction, temperature, density and constant-pressure specific heat capacity. Several formulations for the temperature equation exist ([7–11]), however the formula from Peters [7] is shown in the present work (Eq. (2)). The scalar dissipation rate χ represents the diffusion time scale and is a measure for the departure of the local flame structure from chemical equilibrium. Values of the scalar dissipation close to $\chi = 0$ 1/s are equivalent to the equilibrium solution, whereas higher values for χ induce a larger departure from equilibrium. This characteristic quantity in the description of non-premixed turbulent combustion is also able to describe the extinction limit of the flame. When it reaches the critical value χ_{ex}, the non-equilibrium effects are so dominant that quenching of the flame occurs. A typical profile for the scalar dissipation rate is given by the parametric distribution in Eq. (3) [8].

$$\chi(Z) = \chi_{st}\exp 2\,[erfc^{-1}(2Z_{st})]^2 - 2\,[erfc^{-1}(2Z)]^2 \tag{3}$$

χ_{st} and Z_{st} represent the scalar dissipation and mixture fraction at stoichiometry and $e\,rfc^{-1}$ the inverse of the complementary error function. The boundary value problem defined by Eqs. (1) and (2) can be solved in steady state conditions ($\partial Y_k/\partial t = \partial T/\partial t = 0$)for different values of χ_{st}, resulting in a tabulation of the resulting temperature and species mass fractions for the laminar flamelets: T, $Y_k = f(Z, \chi_{st})$. The assumption of steady-state involved in the steady flamelet model and the use of the stable burning branch does not allow for extinction and re-ignition of the flame, however this does not pose any restrictions for the test cases presented in the present work.

2.2. PDF integration

After the solution of the counterflow diffusion flame using the flamelet equations, a laminar table of the form T, $Y_k = f(Z, \chi_{st})$is obtained, while further quantities such as density, transport properties etc. can be also tabulated since they are simply a function of the gas composition Y_k and the thermodynamic state (h, p).

In order to include the effect of the Turbulence Chemistry Interaction (TCI) on the flamelets, a PPDF integration takes place using the joint PDF $P(Z, \chi_{st})$. In the present study the Favre averaged values for temperature, species mass fractions and heat capacity are calculated according to Eq. (4).

$$\tilde{\varphi} = \int_0^\infty \int_0^1 \varphi(Z, \chi_{st})\cdot P(Z, \chi_{st})\cdot dZd\chi_{st} \tag{4}$$

whereas for the transport properties (viscosity and thermal conductivity) a Reynolds averaging is used as described in Kim et al. [12].

$$\overline{\varphi} = \bar{\rho}\int_0^\infty \int_0^1 \frac{\varphi(Z, \chi_{st})}{\rho(Z, \chi_{st})}\cdot P(Z, \chi_{st})\cdot dZd\chi_{st} \tag{5}$$

$$\bar{\rho} = \frac{1}{\int_0^\infty \int_0^1 \frac{1}{\rho(Z,\chi_{st})}\cdot P(Z, \chi_{st})\cdot dZd\chi_{st}} \tag{6}$$

The assumption of statistical independence can be used to decouple the multidimensional PPDF yielding $P(Z, \chi_{st}) = P(Z)\cdot P(\chi_{st})$. For $P(Z)$, a β-PDF is usually used, the shape of which is determined by the values of $\tilde{Z}$ and its variance $\tilde{Z}''^2$. For $P(\chi_{st})$, a Dirac delta function or a log-normal distribution are implemented [8]. The flamelet calculations (laminar flamelet generation and PDF integration) are usually carried out for several values of pressure, leading to a tabulation of the gas properties as in Eq. (7).

$$\tilde{\varphi} = f(\tilde{Z}, \widetilde{Z''^2}, \tilde{\chi}_{st}, \tilde{p}) \tag{7}$$

2.3. Frozen flamelet

The flamelet equations as well as the governing equations of the counterflow diffusion flame are adiabatic. This means that the resulting profiles for species mass fractions and temperature correspond to a specific adiabatic enthalpy profile. Under the assumption of unity Lewis number this enthalpy profile is described as

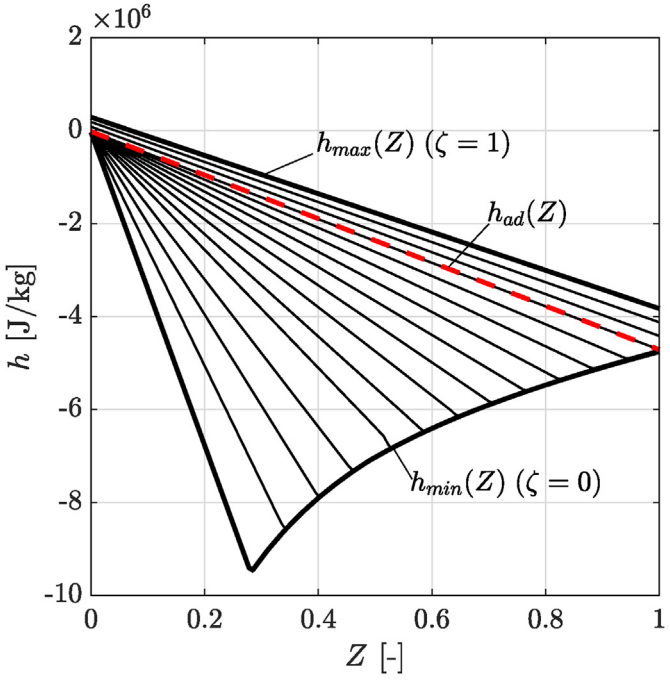

Fig. 2. Enthalpy profiles in mixture fraction space.

$$h_{ad}(Z) = h_{ox} + Z(h_{fu} - h_{ox}) \tag{8}$$

and therefore corresponds to a linear function between the boundary values of fuel and oxidizer. In most engineering applications the flow exchanges heat with its surrounding, and hence not all points of the flow are in adiabatic conditions.

In order to account for the different enthalpy, the usual extension of the adiabatic flamelet model is the concept of frozen flamelet. According to this concept, the species concentrations are assumed to be constant for all enthalpy levels and equal to the concentration at adiabatic conditions. This assumes that the change in enthalpy does not affect the reaction paths in the chemical mechanism and does not change the composition of the gas. The only effect of the non-adiabatic enthalpy level is to change the temperature, the transport and thermodynamic properties of the gas, to render the calculation thermodynamically consistent. Physically it can be interpreted as a cooling down of burned products while ignoring any recombination effects that may take place.

In the presence of cooled walls, which is the case in most rocket engine thrust chamber simulations, this method fails to predict the increase in recombination reactions which occur due to the lower enthalpy environment. The accurate description of the heat flux in the wall requires taking this effect into account and therefore an extension of the flamelet model to non-adiabatic calculations was developed.

3. Non-adiabatic extension of the flamelet model

Several approaches for the extension of the flamelet model to account for non-adiabatic effects have been proposed in the past. Libby et al. [13] used the method of activation energy asymptotics to describe the behavior and characteristics of non-adiabatic flamelets involving counterflowing reactants and products. Lee et al. [14] modeled the wall heat losses by including a source term in the unsteady flamelet equations, thereby introducing a convective heat loss process by means of a Nusselt-number correlation, whereas Fiorina et al. [15] and Cecere et al. [16] used a conductive heat loss approach in burner-stabilized flames. Marracino et al. [17] focused on the effect of radiative losses on the flamelet profiles by adjusting the boundaries of oxidizer and fuel, whereas Orich et al. [18] and Kishimoto et al. [19] reduced the chemical heat source term in the energy equation of the counterflow diffusion flame by a constant factor. Chan et al. [20] employed a radiative source in the flamelet energy equation, while Ma et al. [21] on the other hand applied a modified thermal boundary condition to the counterflow flame in the composition space in the form of a permeable wall. Rahn et al. [22] and Perakis et al. [23] introduced a source term in the energy equation of the counterflow diffusion flame and an iterative approach to obtain the wanted enthalpy levels.

3.1. Enthalpy profiles

To include the effects of sensible enthalpy decrease due to cooled walls and due to expansion in the nozzle, the enthalpy values should be first defined, for which the flamelet table is introduced. For this reason the normalized enthalpy variable ζ can be defined as in the work of Bilger [24]:

$$\zeta = \frac{h - h_{min}(Z)}{h_{max}(z) - h_{min}(Z)} \tag{9}$$

The $h_{max}$and h_{min} profiles ought to be chosen in order to contain all the energy loss or gain within the domain of interest. In the frame of this work, the enthalpy profiles coming from a 1D counterflow diffusion flame with a permeable wall (similar to the work of Ma et al. [21]) are used for the enthalpy deficit levels. The sensitivity of the chosen enthalpy profiles has been examined in the work of Breda et al. [25]. To ensure that all the points in the domain are within the limits of the tabulated enthalpy [22], enthalpy levels above the adiabatic profiles are also included. An example for CH_4/O_2 enthalpy profiles between the h_{max} ($\zeta = 1$) and h_{min} ($\zeta = 0$) lines as well as an adiabatic profile corresponding to $T_{fu} = 270$K and $T_{ox} = 275$ K are shown in Fig. 2.

The non-adiabatic extension of the flamelet model aims at obtaining profiles for mass fractions, temperature and the resulting thermochemical properties of the gas corresponding to enthalpy profiles with heat loss (and heat gain) like the ones in Fig. 2. The tabulation is then a function of the enthalpy as shown in Eq. (10).

$$\tilde{\varphi} = f(\tilde{Z}, \widetilde{Z''^2}, \tilde{\chi}_{st}, \tilde{p}, \tilde{h}) \tag{10}$$

The tabulation as a function of the pressure is justified when the length scale of pressure variations in the combustor is much larger than the flamelet length scale, an assumption which holds when for rocket engines operating in steady state in the absence of combustion instabilities [26].

3.2. Flamelet generation using enthalpy constraint

In the present work, the non-adiabatic extension of the flamelet model is implemented using the prescription of an enthalpy profile as algebraic constraint [12,23]. The idea is based on replacing the energy flamelet equation (Eq. (2)) by imposing an enthalpy profile as an equality constraint in the mixture space frame. By omitting the energy equation, the flamelet calculation is reduced to a boundary value problem consisting of the mass fraction equation (1) and an optimality constraint:

$$h(Z) = h_{tar}(Z) \tag{11}$$

Defining the linear profile of Eq. (8) as the desired enthalpy profile, the set of Eqs. (1) and (11) becomes equivalent to the system of Eqs. (1) and (2). Applying any other profile below (or above) the adiabatic enthalpy, corresponds to a heat loss (or gain) and the equations can be solved without loss of generality.

For the solution of the resulting boundary value problem, a new methodology was implemented based on an operator splitting technique by Strang [27] and Yanenko [28]. The boundary value problem in Eq. (1) consists of a transport term (diffusion term with diffusion constant $\chi/2$) and a non-linear kinetics term. By employing the

operator splitting, the non-linear algebraic equations resulting from the discretization of Eq. (1) are broken into two smaller systems:

- A kinetics equation at each cell in the Z-space, decoupled from other cells (initial value problem)
- A diffusion equation for each chemical species, decoupled from the mass fractions of the other species (parabolic problem)

The solution of the two problems is alternated repeatedly making it possible to match the accuracy of the fully coupled problem. The open-source toolbox Cantera [29] was employed for the chemical calculations and a detailed view of the algorithm is given in Ref. [23].

3.3. Comparison of frozen and non-adiabatic tables

Including non-adiabatic effects in the flamelet table generation enables capturing the effect of reactions occurring at low enthalpy levels. Such reactions are taking place along the cooled walls of rocket combustion chambers and tend to increase the observed heat flux. Specifically, the reduced enthalpy environment suppresses dissociation processes since not enough energy is present to break the chemical bonds. This translates to an increase of recombination processes and a consequent increase in the energy release. This energy release is a result of the lower building enthalpy of the stable products of the recombination reactions. A dominant reaction in the case of hydrocarbon combustion and specifically CH_4/O_2 engines is the recombination of CO to CO_2.

In order to understand the effect of the non-adiabatic flamelet formulation, the results of a frozen chemistry table are compared to the ones from the solution of the enthalpy-dependent flamelets. The load point chosen corresponds to 20 bar CH_4/O_2 combustion and a scalar dissipation rate of 1 s_{-1}. The sub-adiabatic enthalpy levels from Fig. 2 were chosen and for both cases, the chemical mechanism by Slavinskaya et al. [30] was employed.

The temperature results shown in Fig. 3 illustrate the main differences between the two approaches. In the frozen case, an enthalpy reduction has a higher temperature decrement as a consequence. This occurs due to the lower specific heat capacity of the radicals compared to the stable molecules such as CO_2 as well as their enthalpy of formation. In the case of the non-adiabatic model however the heat released from the recombination reactions leads to a smaller temperature decrease in the lower enthalpy levels.

When frozen chemistry is assumed, the lowest enthalpy levels can lead to unphysical temperatures even below 0 K. This is due to the absence of recombination heat release. The species present in the frozen composition cannot exist in such a low enthalpy environment and to avoid that, a temperature cutoff at 100 K was set in the calculation. This explains the flat line at the lowest energy level in the frozen case.

The differences between the two approaches are mainly present close to stoichiometry, whereas for fuel-richer regions the discrepancies are reduced. Since in most practical CH_4/O_2 rocket engine applications the mixture is fuel rich and since in typical co-axial injector configurations the fuel is injected on an outer annulus, the gas composition at the wall is dominantly fuel-rich. The small differences in this region explain why the conventional frozen flamelet model is able to predict reasonable values for the wall heat fluxes when applied in CFD [31].

The results of the species concentrations for different enthalpy levels are shown in Fig. 4. As expected the effect of a lower energy environment is to decrease the composition of CO and increase the CO_2 concentration. The energy release taking place in the recombination is responsible for the temperature difference in Fig. 3.

3.4. Time-scale extension

With the use of the non-adiabatic extension, the prediction of recombination reactions in low-enthalpy environments is possible. In the steady flamelet model however, the deviation from chemical equilibrium is described by the scalar dissipation rate, which is defined as $\chi = 2{\cdot}D(\nabla Z)^2$ in the CFD calculations, with D being the diffusivity. In the vicinity of the walls, as the gradient of the mixture fraction goes towards zero, the scalar dissipation becomes negligible and therefore the mixture will approach the chemical equilibrium solution. This effect leads to a considerable increase in the wall heat loads, as the state of the gas is not necessarily in chemical equilibrium at the wall, especially for low temperatures and slow chemical time-scales. The consequence is that the steady non-adiabatic flamelet model leads to an overprediction of the degree of the recombination in the boundary layer and hence an overestimation of the wall heat loads [22,32].

In order to incorporate the effect of the local chemical time-scale onto the calculation of the mixture composition, a model extension is proposed, which relies on the local Damkoehler number Da defined as the ratio of the flow time-scale τ_f and the chemical time-scale τ_c.

$$Da = \frac{\tau_f}{\tau_c} \tag{12}$$

As the characteristic flow-time scale relevant for the freezing of the

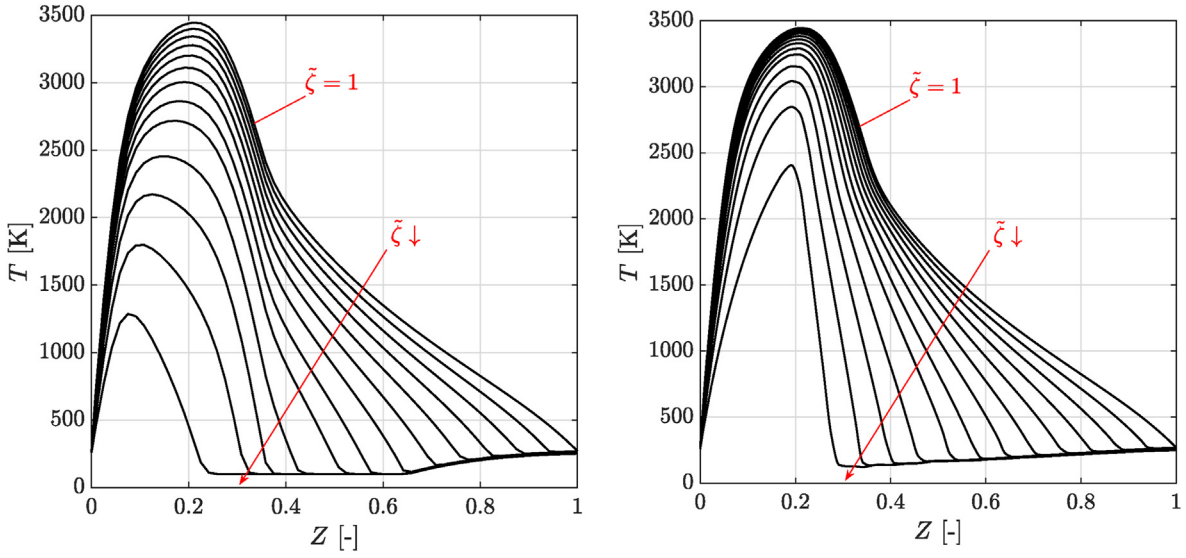

Fig. 3. Temperature profiles for different enthalpy levels in the case of the frozen (left) and non-adiabatic (right) flamelet models.

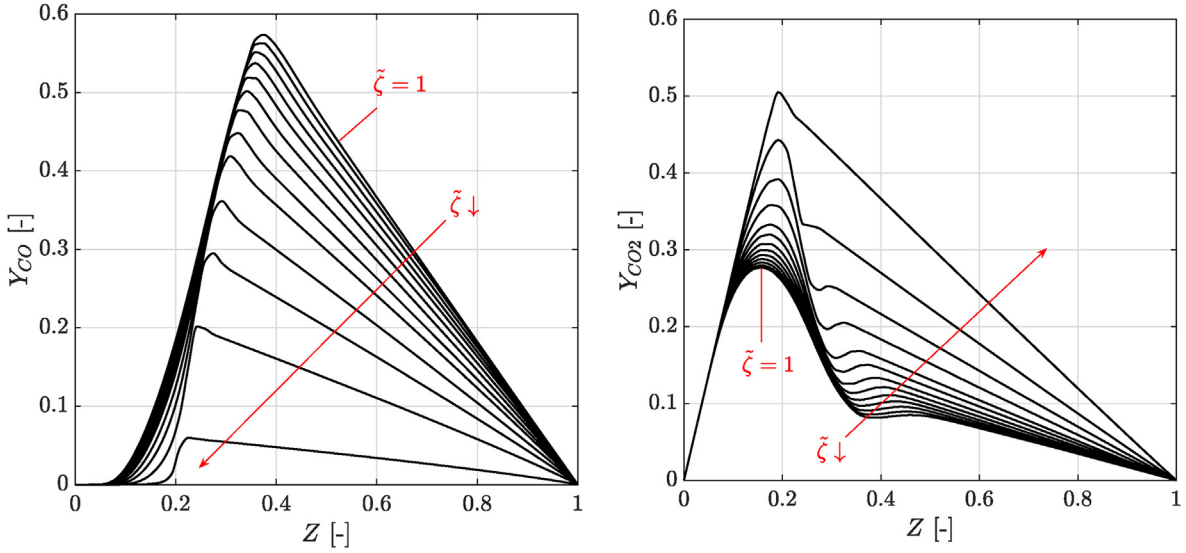

Fig. 4. CO (left) and CO_2 profiles for different enthalpy levels in the non-adiabatic flamelet table.

reactions is the heat transfer through the wall, the definition of τ_f is based on a heat diffusion time-scale equal to $\tau_K \sqrt{Pr}$. In this context $Pr$is the local Prandtl number and $\tau_K$the Kolmogorov scale, as described in Batchelor et al. [33]. For fast chemical time-scales, i.e. large Da, the flow adapts fast to external disturbances and is close to chemical equilibrium conditions [34]. Slower time-scales give rise to low Da and can lead to a frozen chemical composition, where no additional reactions take place. It is expected that for CH_4/O_2 reacting flows close to cooled walls, a freezing of the reactions could occur at the wall. This implies that within the boundary layer the composition will be changing as the distance from the wall decreases, i.e. as the enthalpy is decreasing. When the enthalpy reaches a point where no additional recombinations can occur due to the low temperature, the gas composition remains nearly constant up until the wall. The enthalpy corresponding to the freezing of the reactions is named h_f in the present work.

In the proposed model, the local composition of the gas is frozen when it reaches the freezing enthalpy $h_f$and is simply cooled down to the real enthalpy level h. This means that the species mass fractions Y_i are obtained as a function of the frozen enthalpy

$$\widetilde{Y}_i = f(\tilde{Z}, \widetilde{Z''^2}, \tilde{\chi}_{st}, \tilde{p}, \tilde{h}_f) \tag{13}$$

and the remaining thermochemical quantities (temperature, density, transport properties, heat capacity) are obtained by cooling this composition down to the local enthalpy level

$$\tilde{\varphi} = f(\widetilde{Y}_i, \tilde{p}, \tilde{h}) \tag{14}$$

In order to calculate the freezing enthalpy value as a function of the local enthalpy and the Damkoehler number, following differential equation is solved in an embedded grid along the normal to the wall $\vec{n}$:

$$\frac{\partial h_f}{\partial \vec{n}} = f \cdot \frac{\partial h}{\partial \vec{n}} \tag{15}$$

with the function f describing the effect of the local chemical and flow time-scales on the freezing enthalpy level

$$f = \frac{1 + tanh(\log_{10}(Da))}{2} \tag{16}$$

The equation is solved in the embedded grid with the boundary condition $h = h_f$ at the boundary located away from the wall. For very fast chemical time-scales we obtain $Da > > 1$, leading to $f = 1$. In that case, the frozen enthalpy and the real enthalpy coincide, meaning that no freezing of the reactions occurs. For small values $Da \ll 1$however, the discrepancy between h_f and h increases and the model converges to the frozen flamelet solution.

Several methods for the estimation of the chemical time-scale of a reacting system have been proposed and a useful summary can be found in Prüfert et al. [34] and Fox et al. [35]. In the present study the calculation of the "System Progress Timescale" is undertaken as proposed by Caudal et al. [36] and Prüfert et al. [34]. This is derived from the temporal evolution of the gas composition and temperature in a reacting chemical system, which is given by the ordinary differential equation

$$\frac{\mathrm{d}}{\mathrm{d}t}\begin{bmatrix} Y \\ T \end{bmatrix}(t) = \dot{\omega}(Y, T) = \dot{\omega}\left(Y_1, ..., Y_{N_{sp}}, T\right) \tag{17}$$

with the derivative $\dot{\omega}$ representing the reaction rate. Using a Taylor expansion around the values Y^0, T^0, the temporal evolution of the species reads

$$\frac{\mathrm{d}}{\mathrm{d}t}(Y - Y^0)(t) = J \cdot (Y - Y^0) + \mathcal{O}((Y - Y^0)^2) \tag{18}$$

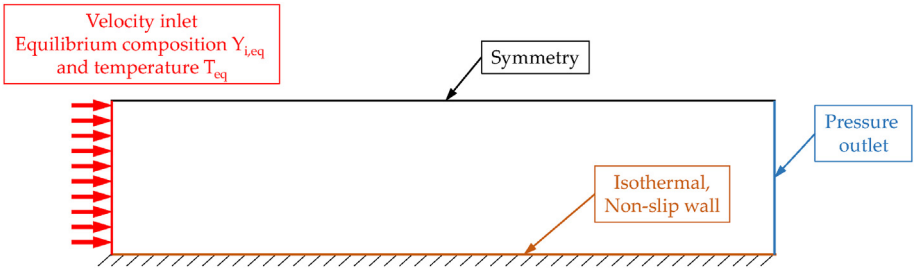

Fig. 5. Schematic illustration of the computational domain for the flat plate simulation.

The Jacobian matrix J is defined with $J := (J_{ik})_{i,k=1,\dots,N_{sp}} = \frac{\partial \dot{\omega}_i}{\partial Y_k}(Y^0)$ and the chemical time-scale τ_c can then be calculated as in Ref. [34] according to Eq. (19).

$$\tau_c = \frac{||\dot{\omega}||}{||J \cdot \dot{\omega}||} \tag{19}$$

The calculation of the chemical time-scale can be performed in situ during the CFD calculation or even tabulated along with the other thermochemical variables of the flamelet model during the pre-processing step.

4. Model Verification

In order to examine the ability of the proposed model to capture recombination effects, a simplified 2D test case of a flat plate is defined. The operating conditions defined for the plate simulation are chosen so as to resemble the flow within rocket combustion chambers. A schematic of the computational domain is shown in Fig. 5. Hot products at adiabatic equilibrium conditions are injected uniformly at the inlet. The temperature of the isothermal plate wall is prescribed at 500 K, while the exit plane is defined as a pressure outlet. The dimensions are chosen with sufficient length to allow for the development of the thermal and species boundary layer. A length of 300 mm and height of 20 mm were used. The flat plate targets the investigation of thermal boundary layer characteristics under rocket thrust chamber operating conditions. As the mixture is injected in pre-burnt conditions, it is possible to isolate the effect of reactions in the vicinity of the wall from other phenomena taking place in the chamber such as mixing and combustion.

For the verification of the model, simulations for several operating points were carried out, for different propellant combinations, mixture ratios, pressure levels and inlet Mach numbers. The variations in those conditions targeted at covering a wide range of possible operating regimes typically found in sub-scale and full-scale rocket thrust chambers. Both CH_4/O_2 and H_2/O_2 mixtures have been examined, with mixture ratios varying from 2.2 to 4.0 for methane and from 4.4 to 8.0 for hydrogen. The pressure range examined was 10–50 bar and Mach numbers between 0.1 and 0.5 were investigated, corresponding to typical contraction ratios found in flight hardware [1].

4.1. Computational setup

A mesh consisting of $50{\cdot}10^3$ finite volumes is used for the simulations, refined in the wall normal direction to ensure that the condition $y^+ < 1$ is satisfied at the wall.

The flowfield in the domain is described by the conservation equations for mass, momentum and energy:

$$\frac{\partial \bar{\rho}}{\partial t} + \frac{\partial (\bar{\rho}\tilde{u}_i)}{\partial x_i} = 0, \tag{20a}$$

$$\frac{\partial (\bar{\rho}\tilde{u}_i)}{\partial t} + \frac{\partial (\bar{\rho}\tilde{u}_i\tilde{u}_j)}{\partial x_j} = -\frac{\partial \bar{p}}{\partial x_i} + \frac{\partial}{\partial x_i}\left(\bar{\tau}_{ij} - \bar{\rho}\widetilde{u_i'' u_j''}\right), \tag{20b}$$

$$\frac{\partial (\bar{\rho}\tilde{h})}{\partial t} + \frac{\partial (\bar{\rho}\tilde{h}\tilde{u}_i)}{\partial x_i} = \frac{\partial}{\partial x_i}\left(\frac{\bar{\lambda}}{\bar{c}_p}\frac{\partial \tilde{h}}{\partial x_i} - \bar{\rho}\widetilde{u_i'' h''}\right), \tag{20c}$$

where $\bar{\rho}$ and $\bar{p}$ are the Reynolds-averaged density and pressure respectively and $\tilde{u}_i$ are the Favre-averaged velocity components in the spatial directions x_i. The viscous stress tensor is $\bar{\tau}$. The specific enthalpy is $\tilde{h}$, $\bar{c}_p$ and $\bar{\lambda}$ are the specific heat and the thermal conductivity of the fluid. NASA polynomials are implemented for the enthalpy and heat capacity of the individual species and a mass-weighting averaging is employed for the mixture values.

A pressure based scheme is used for the solution of the discretized equations with the SIMPLE scheme. Density and pressure are coupled through the ideal gas equation of state:

$$\bar{\rho} = \frac{\bar{p} M}{R\tilde{T}}, \tag{21}$$

where R is the universal gas constant, and $\tilde{T}$ and M are the fluid mixture temperature and molecular weight respectively.

The turbulent momentum flux is modeled employing the Boussinesq hypothesis, relating the Reynolds stresses to the mean velocity gradients:

$$\bar{\rho}\widetilde{u_i'' u_j''} = -\mu_t\left(\frac{\partial \tilde{u}_i}{\partial x_j} + \frac{\partial \tilde{u}_j}{\partial x_i} - \frac{2}{3}\delta_{ij}\frac{\partial \tilde{u}_k}{\partial x_k}\right) + \frac{2}{3}\bar{\rho}\tilde{k}, \tag{22}$$

where μ_t is the turbulent viscosity and k the turbulent kinetic energy. δ_{ij} is the Kronecker delta.

Turbulent closure is achieved by employing the standard k-ε model proposed by Launder and Spalding [37] and using a two-layer approach [38] for the wall. The model allows for the determination of the turbulent length and time scales by solving two additional transport equations for turbulent kinetic energy $\tilde{k}$ and its dissipation $\tilde{\varepsilon}$:

$$\frac{\partial (\bar{\rho}\tilde{k})}{\partial t} + \frac{\partial (\bar{\rho}\tilde{k}\tilde{u}_i)}{\partial x_i} = \frac{\partial}{\partial x_i}\left[\left(\mu + \frac{\mu_t}{\sigma_k}\right)\frac{\partial \tilde{k}}{\partial x_i}\right] + P_k - \bar{\rho}\tilde{\varepsilon} \tag{23}$$

$$\frac{\partial (\bar{\rho}\tilde{\varepsilon})}{\partial t} + \frac{\partial (\bar{\rho}\tilde{u}_i\tilde{\varepsilon})}{\partial x_i} = \frac{\partial}{\partial x_i}\left[\left(\mu + \frac{\mu_t}{\sigma_\varepsilon}\right)\frac{\partial \tilde{\varepsilon}}{\partial x_i}\right] + C_{\varepsilon 1}\frac{\tilde{\varepsilon}}{\tilde{k}}P_k - C_{\varepsilon 1}\bar{\rho}\frac{\tilde{\varepsilon}^2}{\tilde{k}} \tag{24}$$

The turbulent viscosity is then found by the relation $\mu_t = \bar{\rho} C_\mu \frac{\tilde{k}^2}{\tilde{\varepsilon}}$ and all modeling constants are set to the proposed standard values.

The closure of the turbulent heat flux in Eq. (20c) is achieved using the turbulent Prandtl number:

$$\bar{\rho}\widetilde{u_i'' h''} = -\frac{\lambda_t}{\bar{c}_p}\frac{\partial \tilde{h}}{\partial x_i} = -\frac{\mu_t}{Pr_t}\frac{\partial \tilde{h}}{\partial x_i} \tag{25}$$

A constant turbulent Prandtl number equal to 0.9 is chosen throughout the domain. For the molecular transport (viscosity and thermal conductivity) the Chapman-Enskog kinetic theory [39] is utilized for the individual species, combined with the Wilke mixture rule [40], leading to species- and temperature-dependent properties.

For the finite rate calculations, a transport equation for each species mass fraction Y_k is solved, according to:

$$\frac{\partial (\bar{\rho}\tilde{Y}_k)}{\partial t} + \frac{\partial (\bar{\rho}\tilde{u}_i\tilde{Y}_k)}{\partial x_i} = \frac{\partial}{\partial x_i}\left(\left(\rho D_{k,m} + \frac{\mu_t}{Sc_t}\right)\frac{\partial \tilde{Y}_k}{\partial x_i}\right) + M_k\dot{\omega}_k \tag{26}$$

For the calculation of the reaction rates $\dot{\omega}_k$, the chemical mechanism by Slavinskaya et al. [30] is employed in all methane simulations and the chemical mechanism by Ó Conaire et al. [41] for all hydrogen simulations, whereas the diffusivity of each species $D_{k,m}$is calculated according to the kinetic theory [39].

When utilizing the flamelet model, instead of solving $N_{sp} - 1$ transport equations for the N_{sp} chemical species, only one equation for the mixture fraction has to be solved:

$$\frac{\partial (\bar{\rho}\tilde{Z})}{\partial t} + \frac{\partial (\bar{\rho}\tilde{u}_i\tilde{Z})}{\partial x_i} = \frac{\partial}{\partial x_i}\left(\frac{\mu + \mu_t}{Sc_t}\frac{\partial \tilde{Z}}{\partial x_i}\right) \tag{27}$$

where Sc_t is the turbulent Schmidt number which is set to a constant value of $Sc_t = 0.6$ throughout the domain.

Non-equilibrium effects in the flamelet model are included through tabulation dependent on the scalar dissipation:

$$\tilde{\chi} = \frac{C_\chi \tilde{\varepsilon}\widetilde{Z''^2}}{\tilde{k}} \tag{28}$$

where C_χ is a constant with value of 2.0. An additional transport equation is solved for the evaluation of the mixture fraction variance field:

$$\frac{\partial(\bar{\rho}\widetilde{Z''^2})}{\partial t} + \frac{\partial(\bar{\rho}\tilde{u}_i\widetilde{Z''^2})}{\partial x_i} = \frac{\partial}{\partial x_i}\left(\frac{\mu + \mu_t}{Sc_t}\frac{\partial\widetilde{Z''^2}}{\partial x_i}\right) + C_g\mu_t\frac{\partial\tilde{Z}}{\partial x_i}\frac{\partial\tilde{Z}}{\partial x_i} - C_d\bar{\rho}\frac{\tilde{\varepsilon}}{\tilde{k}}\widetilde{Z''^2} \quad (29)$$

where C_g and C_d are constants with values of 2.86 and 2.0 respectively.

For all simulations the commercial code ANSYS Fluent (Version 18.0) was utilized, where the non-adiabatic and the extended non-adiabatic flamelet model were implemented by means of user defined functions.

4.2. Verification results

The results for two representative operating points are shown in the present section. Those correspond to a pressure level of 20 bar and inlet Mach number of 0.2. The mixture fraction for the methane case is chosen at 2.6 and for the hydrogen case at 5.5. For each case, the results form the finite rate simulation (FRC), the frozen flamelet (FRF), the non-adiabatic flamelet model (NAF) and the time-scale extended hybrid model (HYF) are presented. As the FRF model does not account for changes in species composition and since the injection at the inlet occurs at pre-mixed and pre-burnt conditions, the mass fractions remain constant along the wall normal.

Given the absence of exact solutions for the reacting boundary layer over a cooled wall with complex hydrocarbon chemistry the performance of the three flamelet models is assessed based on their ability to reproduce the finite rate results. Since in the finite rate case, the reaction time-scales are resolved and the model has been successfully applied in the past for heat flux estimations in cooled H_2/O_2 and CH_4/O_2 engines [42,43] it is considered to be the baseline reference.

Fig. 6 shows the species and temperature profiles for the flat plate simulations. For the H_2/O_2 simulation, the mass fractions of the major products responsible for the heat release in the boundary layer are plotted, namely H_2O and OH. The temperature profile from the finite rate results is also shown for reference. As the temperature decreases, the OH radical starts recombining forming additional H_2O. The available OH is consumed fast and its mass fraction drops to zero at $y^+ \approx 20$. For positions closer to the wall, both the H_2O and OH concentrations remain constant indicating the ceasing of recombination reactions.

It can be observed that both the non-adiabatic flamelet and the hybrid flamelet model appear to match the finite rate profiles with great accuracy. This is expected as the fast hydrogen chemistry leads to the flow being in chemical equilibrium even at the low temperatures found in the cooled boundary layer. This is confirmed by the Damkoehler number profile shown in the left sub-figure of Fig. 7. As expected, the Damkoehler number qualitatively follows the temperature distribution, having large values further away from the wall, indicating fast reaction rates. As the gas is approaching the wall, the Damkoehler number is reduced but still remains larger than 1 for most of the radial positions. Therefore it is also expected that the deviation between the enthalpy h and the frozen enthalpy h_f is negligible as demonstrated in the same figure.

The corresponding CH_4/O_2 results on the other hand are showing a larger discrepancy between the sub-models. The CO/CO_2 equilibrium is defining the bulk energy release within the reacting boundary layer [23] and therefore the mass fractions of those two species are plotted along the wall normal. As the temperature is reduced closer to the wall, CO is converted into CO_2, which is predicted by all three models (FRC, NAF, HYF). For radial positions larger than $y^+ \approx 40$ the three models seem to produce identical results. The non-adiabatic model however appears to over-predict the degree of conversion of CO compared to the finite rate model closer to the wall. Whereas FRC predicts that a ceasing of reactions takes place at T≈1500 K ($y^+ \approx 30$), the concentration of CO_2 keeps increasing for the NAF, even at temperatures below 800 K. This is largely attributed to the fact that for pre-burnt configurations the scalar dissipation rate is 0, meaning that the non-adiabatic flamelet degenerates to the equilibrium model. Slow processes like the conversion of CO to CO_2 are hence over-predicted.

The HYF model on the other hand closely follows the FRC and also predicts a steep reduction of the recombination reactions for $y^+ < 30$. This is explained by the Damkoehler number profile shown in Fig. 7. Similar to the H_2/O_2 case, the Damkoehler number reduces with increasing proximity to the wall, but the absolute level is lower reflecting the slower chemical time-scales [44]. The fact that the Damkoehler number reaches values as low as 10^{-3} implies that there is a large deviation between the enthalpy and the frozen enthalpy. This growing difference becomes significant for positions with $y^+ < 30$, coinciding with the freezing of the reactions in Fig. 6.

It is hence evident that the proposed extension for the non-adiabatic flamelet model is able to capture both the initiation of the recombination reactions within the thermal boundary layer as well as the ceasing of the aforementioned reactions in areas with very low enthalpy. Considering the verification of the model based on the presented flat plate simulation, a more complex rocket combustor test-case with available experimental data is chosen to evaluate the performance of the proposed model.

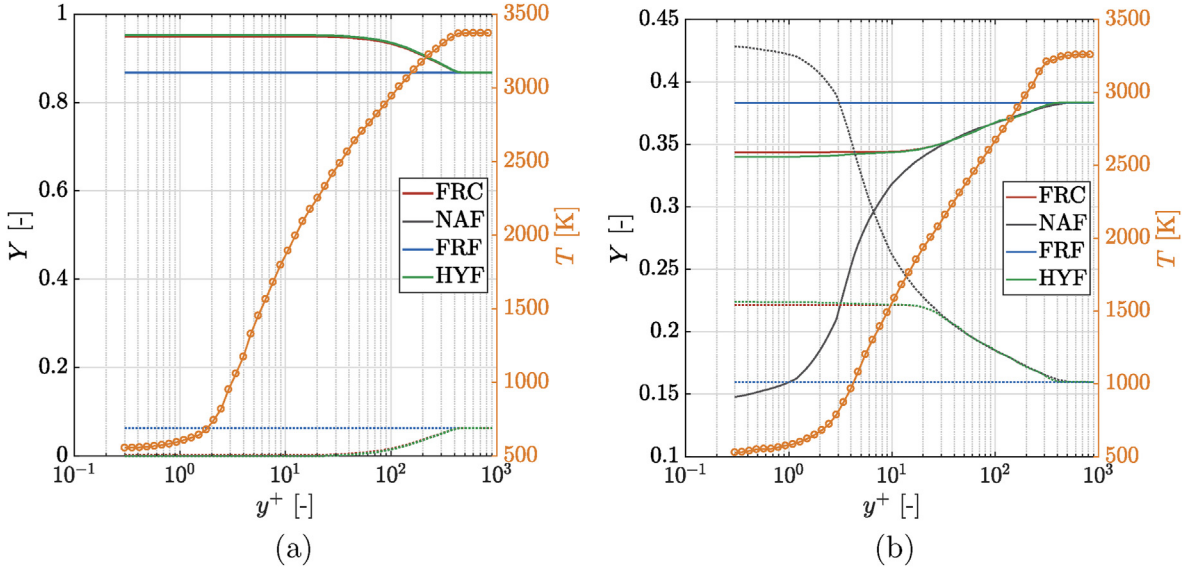

Fig. 6. Species profiles along wall normal at $Re_x = 75{\cdot}10^5$ for the H_2/O_2 (a) and the CH_4/O_2 (b) flat plate simulation.

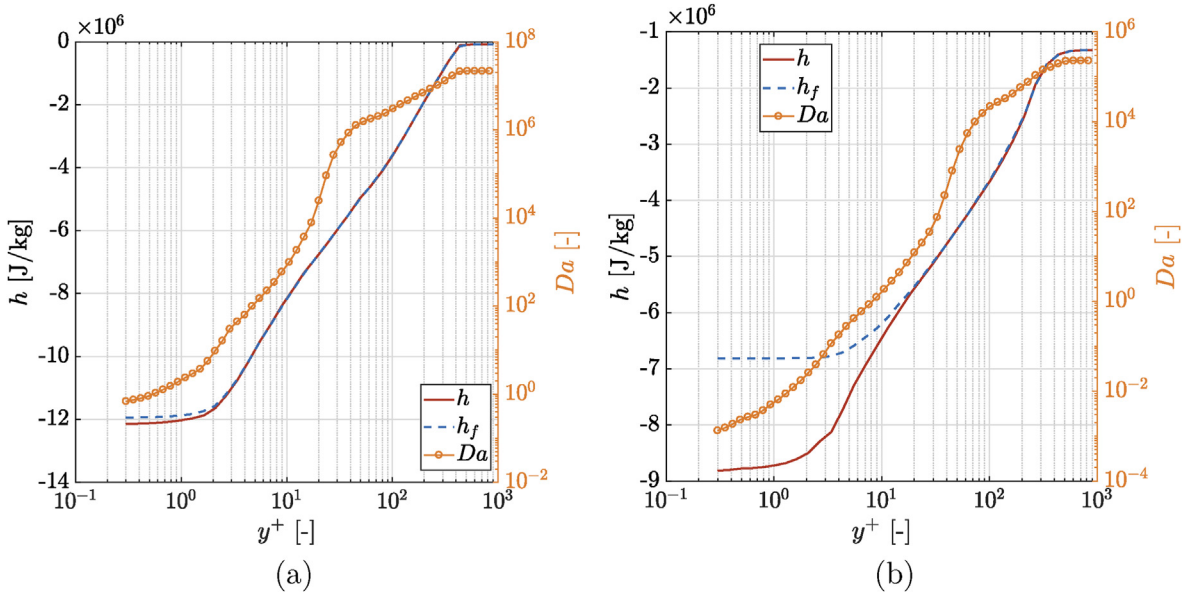

Fig. 7. Enthalpy and Damkoehler number profiles along wall normal at $Re_x = 75{\cdot}10^5$ for the H_2/O_2 (a) and the CH_4/O_2 (b) flat plate simulation.

5. Simulation of a single element rocket combustor

To assess the effects of the wall heat transfer on the flow-field structure and the performance of the extended non-adiabatic flamelet combustion model, RANS calculations of a single-element rocket combustor are carried out.

5.1. Experimental configuration

The single-element rocket combustor experimentally investigated by Silvestri et al. [45] is used for this analysis. The experimental configuration is illustrated in Fig. 8 and consists of the main rocket chamber having a diameter of 12 mm and the convergent-divergent nozzle with an contraction ratio of 2.5. Two propellant feed lines supply gaseous fuel and oxidizer to the coaxial injector. The facility has the capability of operating with both methane and hydrogen as fuel at ambient temperature. The central injector nozzle has a diameter of 4 mm whereas the fuel is supplied by an annulus surrounding the inner oxidizer stream, with inner and outer diameters of 5 and 6 mm respectively. The post separating the fuel and oxidizer stream is not recessed with respect to the injector face-plate. An operating point corresponding to a nominal chamber pressure of 20 bar has been chosen with an oxidizer to fuel ratio equal to 2.22 for the methane case. In order to demonstrate the capabilities of the non-adiabatic model to properly capture the combustion dynamics of not only $CH2/O_2$ but also H_2/O_2, the results for a load point at 20 bar with O/F = 5.85 using hydrogen as fuel is also shown. The inlet conditions for both operating points are given in Table 1.

5.2. Computational setup

The equations used for the simulation of the flowfield in the combustion chamber are already described in Section 4.1. In order to take advantage of the symmetry in the RANS simulation, a 2D axisymmetric domain is chosen consisting of the coaxial injector, combustion chamber and nozzle. The mesh consists of 75000 cells and part of it is shown in Fig. 9. At all walls, the $y^+ < 1$ condition holds.

The mass flow and temperature is defined at the inlet boundaries for oxygen and methane, whereas a pressure outlet is applied at the exit plane. The experimental temperatures obtained with an inverse method [46] are applied at the walls along with a no-slip condition.

The mesh was chosen after an extensive grid convergence study. As characteristic quantities, the maximal wall pressure p_{max} and maximal heat flux at the combustion chamber wall $\dot{q}_{max}$ (excluding the nozzle), as well as the integrated wall heat loss $\dot{Q}$, are considered for a simulation using the frozen flamelet model. To assess the convergence of the solution, the theory of the Richardson extrapolation [47] as well as the CGI approach advocated by Roache [48] were employed. The CH_4/O_2 frozen flamelet simulation was used for this analysis.

The numerical error is calculated by comparing the solutions on each grid to a value gained from Richardson extrapolation according to

$$\varphi_{ext} = \varphi_1 + \frac{\varphi_1 - \varphi_2}{r^{\psi} - 1} \tag{30}$$

where the lower indices represent the finer mesh solutions and r is the grid refinement ratio.

The results are summarized in Table 2, whereas Fig. 9 shows the numerical error as a function of the grid points. All simulations were carried out with a second order upwind scheme for all transport equations. The achieved order ψ of convergence was also estimated for each of the three variables, using the method shown in Eq. (31).

$$\psi = \frac{\log \frac{\varphi_3 - \varphi_2}{\varphi_2 - \varphi_1}}{\log r} \tag{31}$$

For the integrated heat loss, maximal pressure and maximal heat flux, apparent orders of 2.40, 2.48 and 3.28 were obtained. The relative numerical errors for the middle grid remain underneath 1.5% whereas the GCI is below 10% using the conservative formulation by Roache

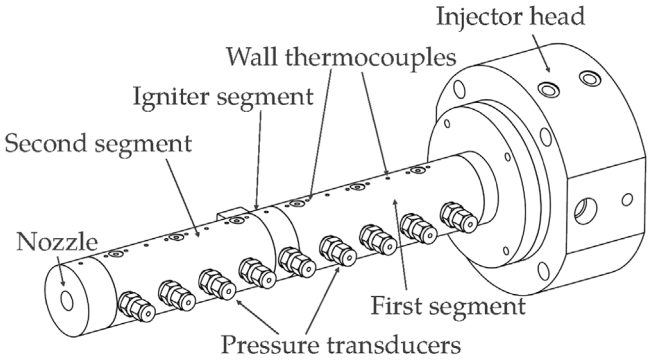

Fig. 8. Sketch of the single-element combustor.

Table 1
Summary of the experimental load points.

Case	H_2/O_2	CH_4/O_2
Nominal pressure [bar]	20	20
Mixture ratio O/F [−]	5.85	2.22
Mass flow rate fuel [g/s]	5.65	15.30
Mass flow rate oxidizer [g/s]	32.99	33.97
Fuel inlet temperature T_{fu} [K]	282	276
Oxidizer inlet temperature T_{ox} [K]	279	278
Velocity ratio u_{fu}/u_{ox} [−]	4.22	1.29

Table 2
Results of the grid convergence study.

	Coarse	Middle	Fine
Cells [−]	58000	75000	97500
r [−]	1.3	1.3	
$\dot{Q}$ [kW]	45.22	45.82	46.14
$\varepsilon_{\dot{Q}}$ [%]	2.77	1.47	0.79
p_{max} [bar]	19.12	19.35	19.47
$\varepsilon_{p_{max}}$ [%]	2.45	1.28	0.67
$\dot{q}_{max}$ [MW/m^2]	6.78	6.91	6.96
$\varepsilon_{\dot{q}_{max}}$ [%]	3.21	1.36	0.58
GCI$\dot{Q}$ [%]	8.42	1.87	
GCIp_{max} [%]	7.46	1.62	
GCI$\dot{q}_{max}$ [%]	9.78	1.72	

[48]. For that reason, the middle mesh was chosen for all simulations presented in this work.

It is important to note that in the case of simulations of reacting flows, apart from the sufficiently fine mesh, the effect of accumulated error due to numerical integration of the chemical source term, also has to be quantified, similar to the work by Smirnov et al. [49,50]. However, since the RANS equations are solved in the present work, where no explicit dynamic integration takes place, the issue of error accumulation is not relevant in this case.

5.3. Results

5.3.1. H_2/O_2 test case

Based on the results of the verification test case and the finding that NAF and HYF produce almost identical results, only the results of the hybrid model are discussed here (see Fig. 12).

Fig. 10 shows the temperature field within the chamber. A thin reaction zone appears in the shear layer of the co-axial injector which expands radially with increasing axial position. At approximately $x = 120$mm the flame reaches the wall and after this point the thermal boundary layer starts growing, indicated by a thin low-temperature zone in the vicinity of the wall. The stoichiometric line, which can be used to infer the flame length of the injector, appears to extend until $x = 140$mm. After this axial position, the temperature field is mainly homogeneous meaning that the bulk energy release due to combustion is completed. This is confirmed by the heat flux profiles in Fig. 13 which will be discussed later. The short length of the flame (compared to the total combustor length) can be explained by the large velocity ratio and the fast chemical time-scales of the H_2/O_2 combustion. A velocity ratio of 4.22 (Table 1) is responsible for a strong shear interaction close to the injector and an efficient turbulent mixing. The energy release is also taking place fast due to the small chemical scales represented by the Damkoehler values in Fig. 10. The Damkoehler number is larger than 10_6 for the majority of the flow indicating chemical equilibrium conditions. The greyed areas correspond to regions with more than 90% fuel or oxidizer, where the definition of the chemical time-scale becomes ill-posed.

The corresponding mass fractions fields for the species H_2O and OH can be found in Fig. 11. Since H_2O is the major product of H_2/O_2 combustion it reaches concentrations of up to 90% in the chamber and is mainly produced in areas with high temperature, where the main heat release takes place. Also it appears to build up close to the wall where the recombination reactions are induced due to the low enthalpy. The recombination reactions are clearly seen in the OH field as well, the concentration of which is clearly reducing in the thermal boundary layer.

A closer inspection is given in Fig. 11, where the species mass fraction and the temperature are plotted along the wall normal. For the $x = 100$mm axial position the combustion is not completed and hence low product concentrations occur close to the chamber axis ($y^+ > 10^3$). Moving closer to the wall, both the H_2O and OH mass fractions increase within the reacting shear layer. Finally for positions within the boundary layer ($y^+ < 10^2$) the OH concentration is reduced to zero, as it completely recombines to form water molecules. The profiles for $x = 200$mm are qualitatively very similar since a full recombination of OH to H_2O occurs within the thermal boundary layer. The only difference is that the flow mainly consists of pre-burnt products even close to the chamber axis and hence resembles the flat-plate results from Section 4.

The comparison of the simulation results with the available experimental pressure and heat flux data is carried out in Fig. 13. The absolute pressure level seems to be accurately captured by the HYF model, meaning that it is able to correctly predict the combustion efficiency. The pressure drop profile in the chamber is also an indicator

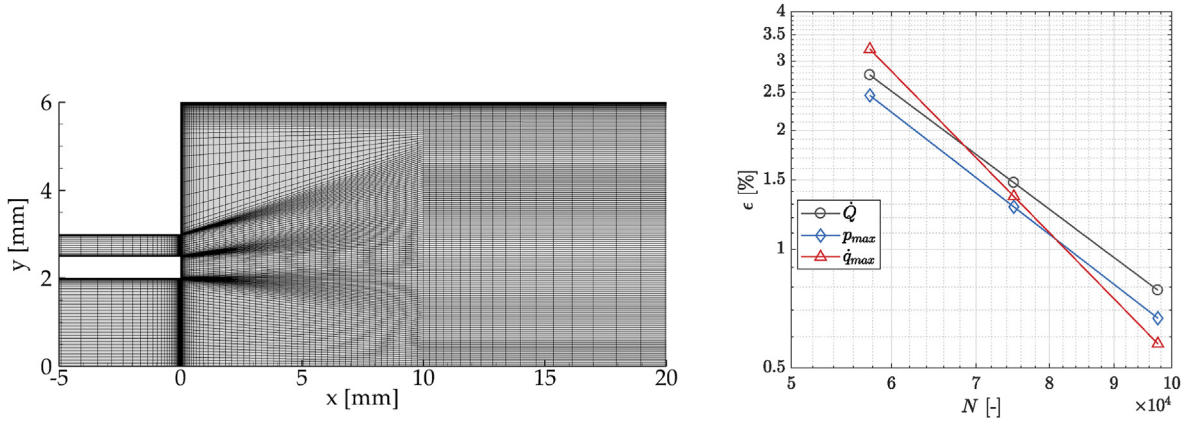

(a) Mesh in the vicinity of the injector. (b) Mesh convergence study.

Fig. 9. Mesh and numerical error as a function of the grid point number.

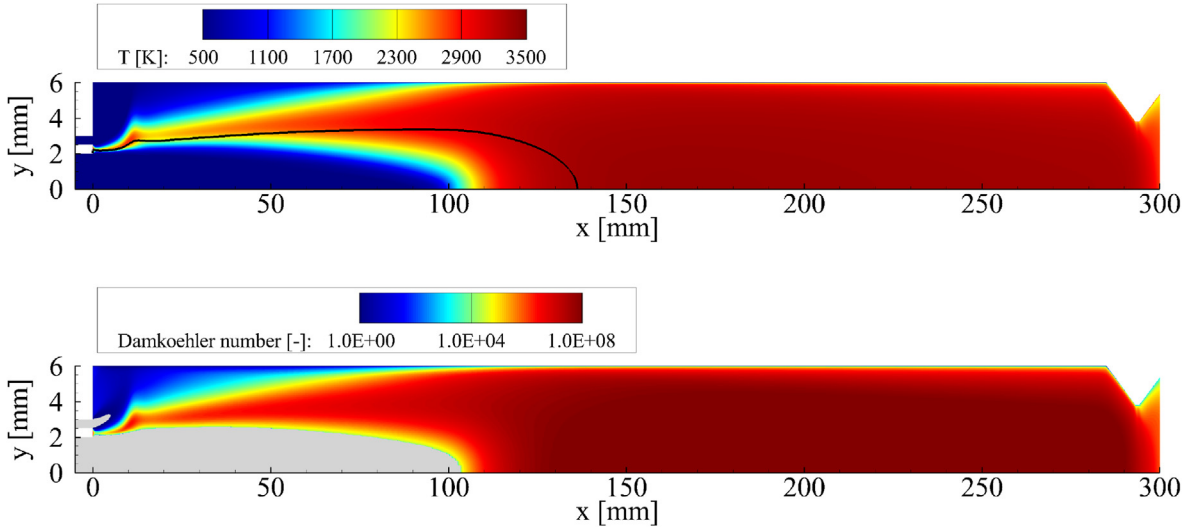

Fig. 10. Temperature (top) and Damkoehler number (bottom) fields for the H_2/O_2 simulation. The black line corresponds to the stoichiometric composition $Z_{st} = 0.111$.

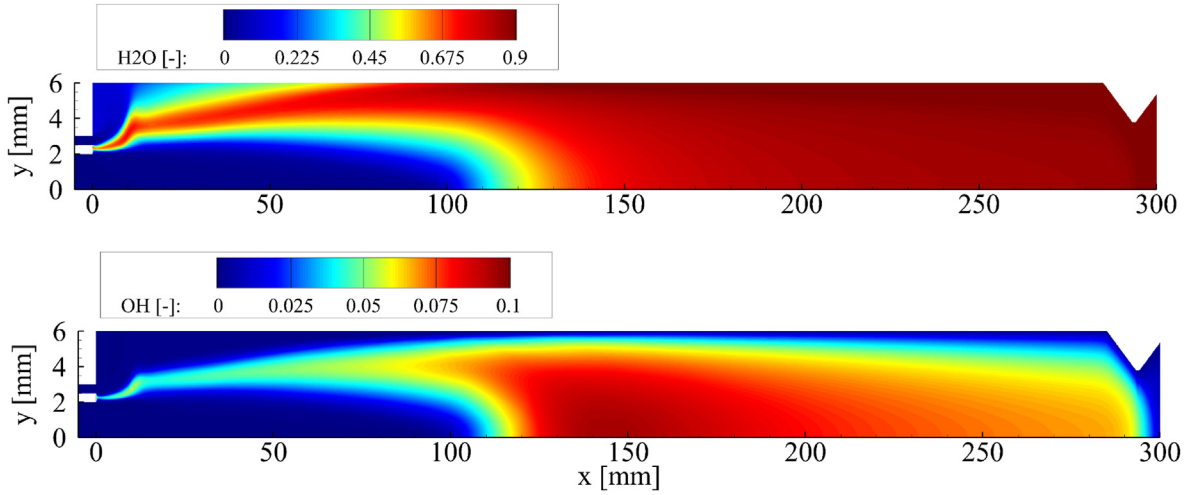

Fig. 11. H_2O (top) and OH (bottom) mass fraction fields for the H_2/O_2 simulation.

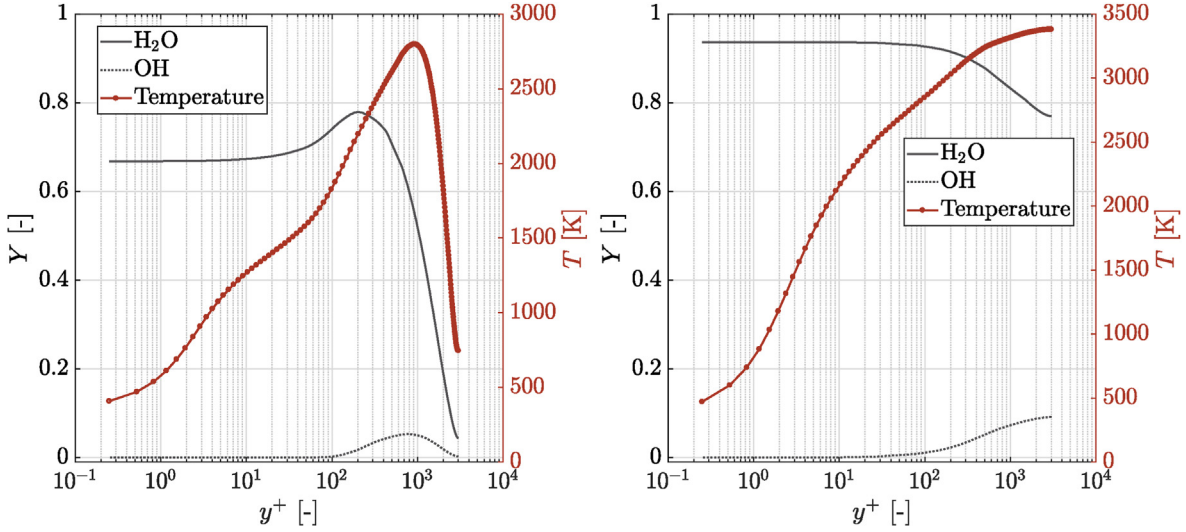

Fig. 12. Species profiles along the wall normal at x = 100 mm (left) and x = 200 mm (right) for the H_2/O_2 simulation.

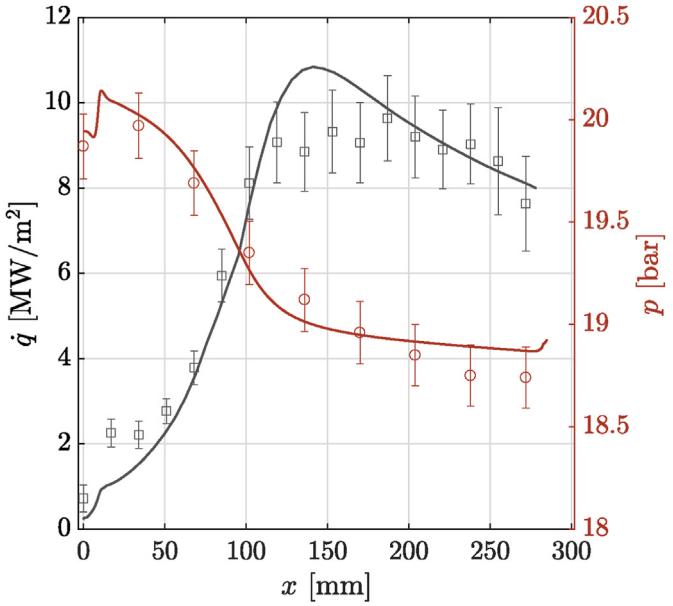

Fig. 13. Heat flux as well as pressure profiles for the H_2/O_2 simulation.

for the energy release in the chamber as it reflects the acceleration of the flow. The HYF model seems to also match the experimental pressure drop quite well. For the first 100 mm the discrepancies between simulation and experiment are minimal. Shortly before the end of the chamber, the numerical results show a flatter profile than the measured values but still within the experimental uncertainty.

A similar situation is found for when examining the wall heat flux data. The absolute heat flux level is captured with good accuracy and the profile follows the experimental measurements with small deviations. Within the recirculation zone close to the face-plate (x<50 mm), the heat flux shows a local maximum due to the stagnation flow of the reacting shear layer onto the wall. Although the simulation also displays a rise in heat flux, this is under-predicted compared to the experimental values. This difference can be attributed to the choice of the turbulence model. Since the impinging flow in the stagnation point is not isotropic, the choice of the $k-\varepsilon$ model is not ideal for capturing it. More complex RANS turbulence closure models or scale-resolving simulations would be required for this region. However, after the short recirculation zone, a steep increase in the heat flux takes place, corresponding to the position where the flame comes in contact with the wall. This is precisely re-produced in the numerical results. After the end of the bulk heat release (at $x \approx 140$mm) the heat flux reaches a plateau in the experiments and seems to drop in the simulation. The agreement of the profiles in the second half of the combustor is still satisfactory with deviations smaller than 1 MW/m^2 occurring throughout the length of the engine.

5.3.2. CH_4/O_2 test case

The results for the methane test case are presented in this section. The temperature distribution in the thrust chamber with the stoichiometric line is given in Fig. 14. Similar to the H_2/O_2 case, the temperature is high within the shear layer between the two propellants and becomes more uniform with increasing distance from the injector. A longer flame is observed compared to the hydrogen case, with the stoichiometric line extending up until $x \approx 200$mm. After this location the flow is homogeneous and no significant heat release is taking place, meaning that the flow is cooled down due to heat losses via the wall.

Lower values for the Damkoehler number are also observed throughout the thrust chamber. This is attributed both to the lower combustion temperature of the methane operating point and the slower chemical processes taking place in hydrocarbon combustion.

Only the HYF temperature results are shown in Fig. 14 since the temperature differences between the individual combustion models outside of the near-wall region are difficult to distinguish. The differences in the composition of the major species however for the three flamelet models are more obvious and are illustrated in Fig. 15. It is important to note that all three models show almost identical results in the regions with adiabatic conditions (i.e. in the main core of the flow) and only deviate in the low-enthalpy environments: the thermal boundary layer and the nozzle.

In the FRF results, CO dominates the region closer to the wall, whereas CO_2 is mainly concentrated in the energy release zone close to the chamber axis. This can be explained by the configuration of the injector, which has the fuel flowing through an outer annulus leading to fuel-rich conditions directly at the wall. For large radial positions therefore, in the absence of enough oxygen, CO_2 cannot be formed and hence CO is the final product. This segregation of the regions where CO or CO_2 are dominant is common in all three models.

The major difference is the heat loss-induced recombination directly at the wall for the NAF and HYF models, where the formation of a thin species boundary layer is evident. CO is oxidated to form CO_2 directly at the wall, a phenomenon which is expected based on previous studies regarding methane engines [44]. Although the NAF and HYF fields appear to be almost identical, large differences occur within the boundary layer.

Fig. 16 elaborates on those discrepancies by showing the species

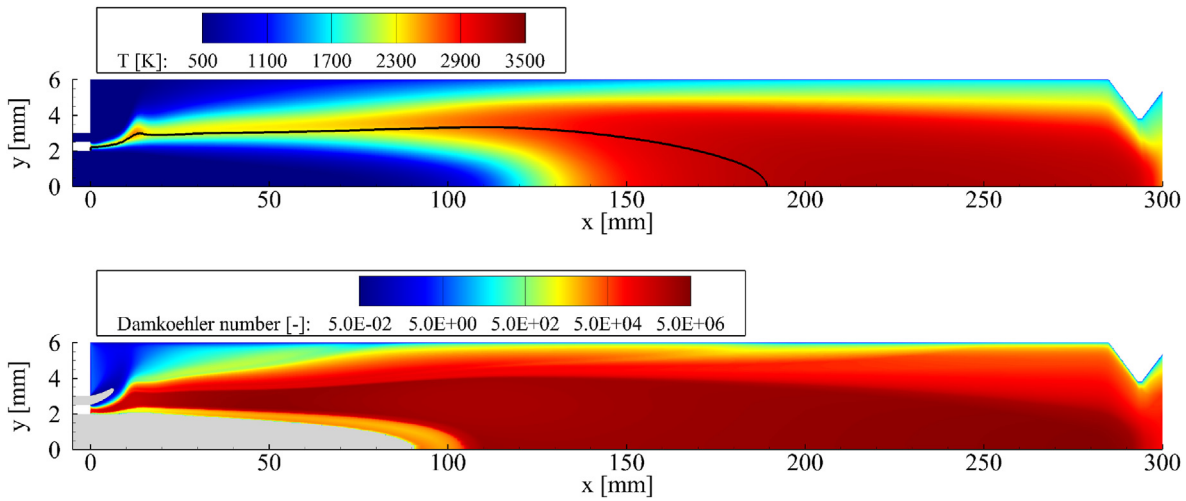

Fig. 14. Temperature (top) and Damkoehler number (bottom) fields for the CH_4/O_2 simulation. The black line represents the stoichiometric composition $Z_{st} = 0.2$.

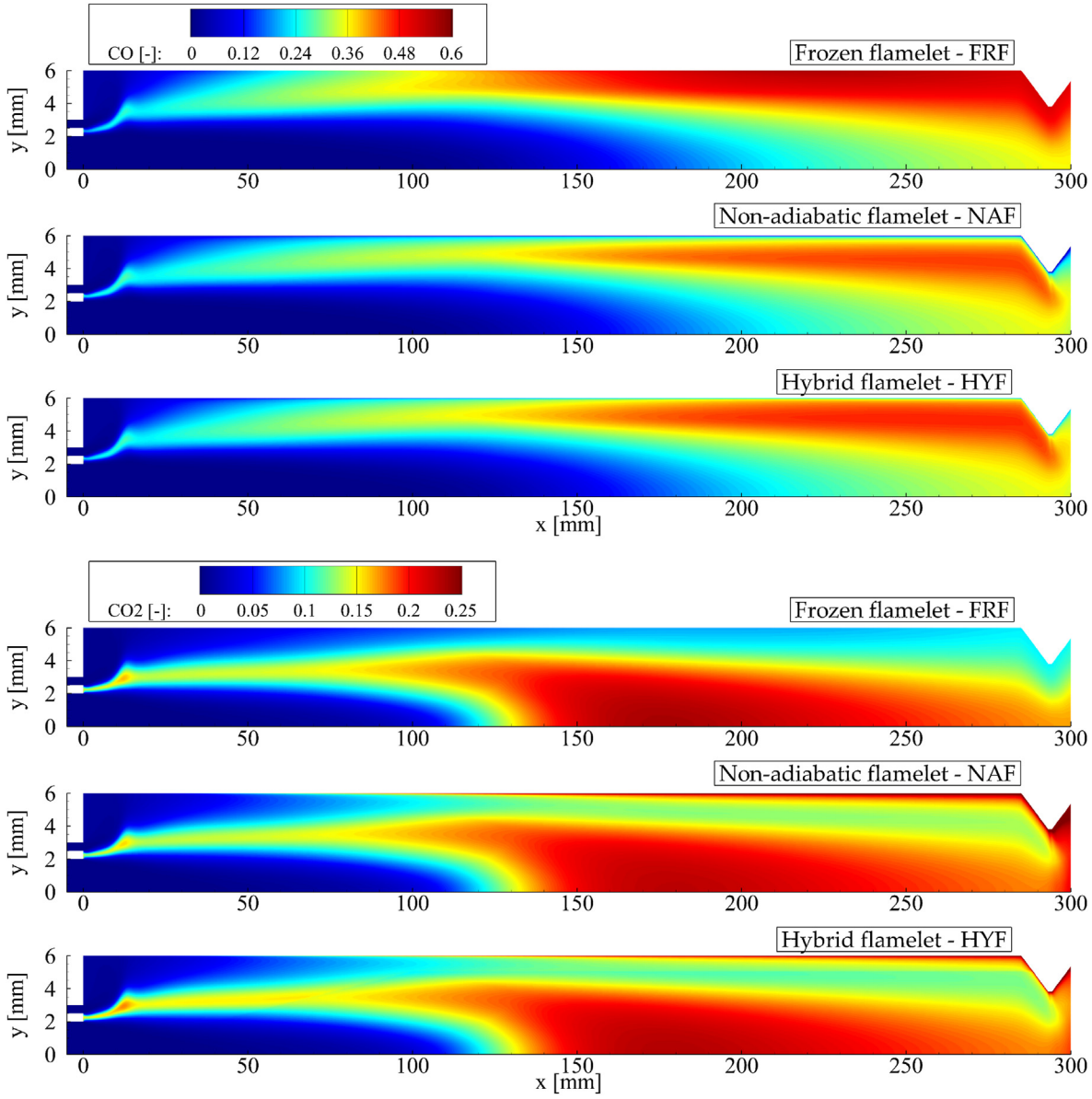

Fig. 15. CO (top) and CO_2 (bottom) species mass fraction fields for the three flamelet models.

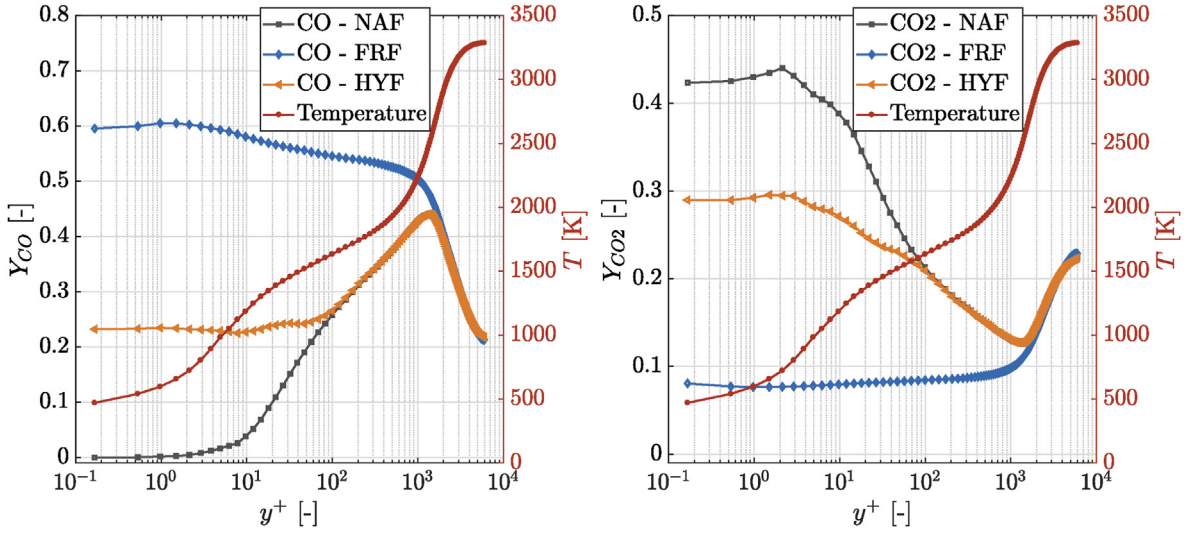

Fig. 16. CO (left) and CO_2 (right) species mass fractions along the wall normal at x = 200 mm for the CH_4/O_2 simulation.

profiles along the wall normal for $x = 200$mm. The temperature profile is also plotted as a reference. Close to the chamber axis ($y^+ > 10^3$) all three models predict nearly identical species distributions, whereas in the presence of the lower temperature environment the NAF and HYF predict the start of recombination reactions. Although the presence of those recombinations which is physically intuitive is present for both models, the degree of recombination shows some significant differences. Specifically, the conversion of CO to CO_2 in the NAF model continues even when the temperature drops below 1000 K within the viscous sub-layer. The reactions cease only when the CO is depleted and reaches a concentration of 0. The HYF model on the other hand restricts the progress rate of the CO to CO_2 conversion at $y^+ \approx 110$.

This can be attributed to the profile of the Damkoehler number shown in Fig. 17. As the chemical time-scales become larger the frozen enthalpy starts deviating from the look-up enthalpy of the flamelet tables and leads to am effective ceasing of additional reactions.

The large effect that the species concentration has on the experimentally measured values (pressure and wall heat flux) can be deduced by looking at Fig. 18. Starting with the wall heat flux in the right subfigure, the results show an expected trend: the frozen model exhibits the lowest absolute heat flux value as it does not predict any additional exothermic reactions induced by the low-enthalpy environment. The non-adiabatic model includes the aforementioned reactions but seems to excessively over-predict them, thereby leading to very large heat flux values. The results of the hybrid model on the other hand display an increased heat flux level compared to the frozen model but still in good agreement with the experimental results. Both the frozen and the hybrid model match the experimental data within 10% which is smaller than the measurement uncertainty. This means that the performance of the frozen model for the prediction of the heat flux is comparable to the hybrid one although it has an unphysical species distribution close to the wall. This explains why the frozen model has been used with success in predicting the wall heat transfer of hydrocarbon engine in the past [31].

A large difference however is evident in the pressure profile (left sub-figure) which proves the superiority of the hybrid model. Both the frozen model and the non-adiabatic model under-predict the pressure level in the combustion chamber, whereas the agreement of the hybrid model with the experimental data is very good.

To understand the reason that the NAF and FRF fail to accurately predict this performance parameter, one has to examine the total energy flow within a typical rocket engine. The energy which is released due to the reactions increases the gas temperature and can be used for either increasing the performance (higher pressure level) or can escape through the chamber walls. In the absence of sufficient heat release, the combustion pressure does not increase up to the expected level. At the same time, an excessive heat release directly at the wall increases the heat loss, thereby removing energy from the core and effectively dropping the pressure again. A predictive numerical tool hence can only be successful when it can get this energy balance correct.

It is obvious that the recombination reactions lead to a non-negligible energy release, which in turn increases the performance (pressure) of the engine. The failure of the frozen flamelet to capture those reactions explains the poor pressure prediction. The non-adiabatic model over-predicts those reactions and leads to excessive heat loss through the walls and a subsequent decrease in performance.

6. Conclusions

The current work introduces a method for extending the classic flamelet model in order to account for non-adiabatic effects. With this extension, species compositions, wall heat transfer and chamber pressure predictions can be carried out without the need for computationally expensive models based on finite rate.

For the generation of the non-adiabatic tables, an enthalpy-prescription method has been proposed. The species equations for a laminar counterflow diffusion flame are solved for different pressure, scalar dissipation and enthalpy profiles. The analysis of the flamelet tables shows that the most significant effect of the lower-enthalpy environment is that it increases the conversion of CO to CO_2.

In order to avoid an excessive predictions of the recombination reactions at the wall, the local chemical time-scale has been introduced. By pre-tabulating the chemical time-scale within the look-up table, the local Damkoehler number of the flow is obtained. Based on the value of the Damkoehler number, the reactions are defined as frozen or continue to evolve.

To verify the results of the new model, the simulation of a reacting flow over a cooled flat plate has been carried out and compared to finite rate results. Both for H_2/O_2 and CH_4/O_2 mixtures the new hybrid model exhibited great agreement with the finite rate results.

The hybrid model has been applied to the simulation of a single-element rocket combustor in realistic operating conditions. For both the H_2/O_2 and CH_4/O_2 cases, a great agreement for the wall heat flux values and pressure level is found. Without the Damkoehler number extension, the non-adiabatic flamelet model leads to an over-prediction of the heat losses through the wall and a subsequent under-prediction of the pressure level, whereas the frozen model shows a sufficiently accurate heat flux prediction but an under-estimation of the pressure level due to the absence of the exothermic recombination reactions. It is hence concluded that the correct prediction of the recombination reactions at the wall is important for the calculation of the performance and wall loads in rocket engines and that the higher fidelity hybrid model is able to capture them with minimal computational cost.

Declaration of competing interest

The authors declare that they have no known competing financial interests or personal relationships that could have appeared to influence the work reported in this paper.

Acknowledgments

Financial support has been provided by the German Research Foundation (Deutsche Forschungsgemeinschaft - DFG) in the framework of the Sonderforschungsbereich Transregio 40: ”Technological Foundation for the design of thermally and mechanically high loaded

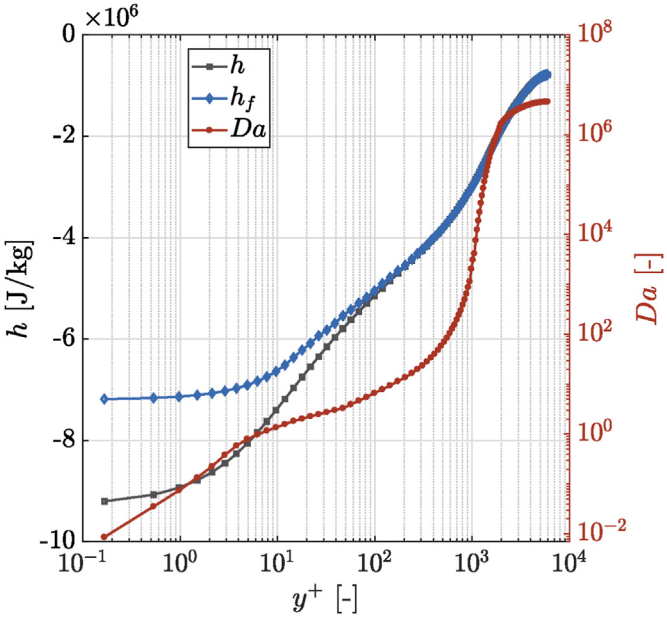

Fig. 17. Enthalpy and Damkoehler number profiles along wall normal at x = 200 mm for the CH_4/O_2 rocket combustor.

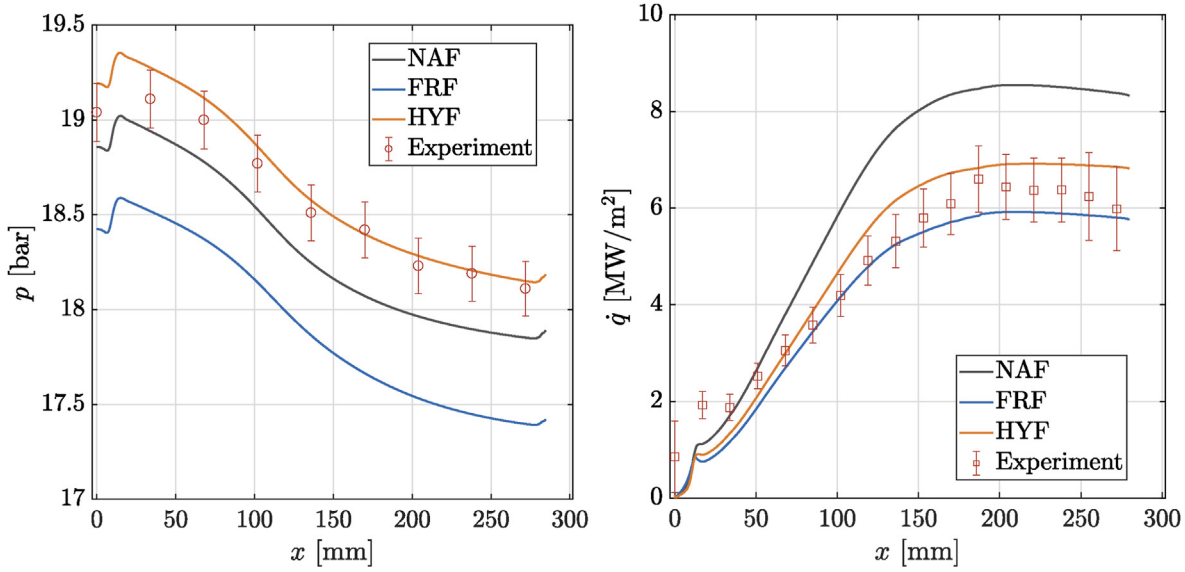

Fig. 18. Pressure (left) and wall heat flux (right) profiles along the axial direction for the CH_4/O_2 rocket combustor.

components of Future Space Transportation System". The authors gratefully acknowledge the Gauss Centre for Supercomputing e.V. (www.gauss-centre.eu) for funding this project by providing computing time on the GCS Supercomputer SuperMUC at Leibniz Supercomputing Centre (www.lrz.de).

References

[1] G.P. Sutton, O. Biblarz, Rocket Propulsion Elements, John Wiley & Sons, New York, 2016.
[2] G.P. Sutton, History of Liquid Propellant Rocket Engines, AIAA, 2006.
[3] D.R. Bartz, A simple equation for rapid estimation of rocket nozzle convective heat transfer coefficients, J. Jet Propuls. 27 (1957) 49–51, https://doi.org/10.2514/8.12572.
[4] P. Gerlinger, Investigation of an assumed pdf approach for finite-rate chemistry, Combust. Sci. Technol. 175 (5) (2003) 841–872, https://doi.org/10.1080/00102200302410.
[5] S.B. Pope, Pdf methods for turbulent reactive flows, Prog. Energy Combust. Sci. 11 (2) (1985) 119–192.
[6] N. Peters, Laminar diffusion flamelet models in non-premixed turbulent combustion, Prog. Energy Combust. Sci. 10 (3) (1984) 319–339, https://doi.org/10.1016/0360-1285(84)9011-X.
[7] N. Peters, Laminar flamelet concepts in turbulent combustion, Symposium (International) on Combustion, vol. 21, Elsevier, 1988, pp. 1231–1250, , https://doi.org/10.1016/S0082-0784(88)80355-2.
[8] N. Peters, Turbulent Combustion, Cambridge University Press, Cambridge, 2000.
[9] H. Pitsch, N. Peters, A consistent flamelet formulation for non-premixed combustion considering differential diffusion effects, Combust. Flame 114 (1–2) (1998) 26–40, https://doi.org/10.1016/S0010-2180(97)00278-2.
[10] S.-K. Kim, S.-M. Kang, Y.-M. Kim, Flamelet modeling for combustion processes and NOx formation in the turbulent nonpremixed CO/H2/N2 jet flames, Combust. Sci. Technol. 168 (1) (2001) 47–83, https://doi.org/10.1080/00102200108907831.
[11] H. Pitsch, H. Barths, N. Peters, Three-dimensional modeling of NOx and soot formation in DI-diesel engines using detailed chemistry based on the interactive flamelet approach, SAE Technical Paper, Society of Automotive Engineers International, 1996, , https://doi.org/10.4271/962057.
[12] S.-K. Kim, M. Joh, H.S. Choi, T.S. Park, Multidisciplinary simulation of a regeneratively cooled thrust chamber of liquid rocket engine: turbulent combustion and nozzle flow, Int. J. Heat Mass Tran. 70 (2014) 1066–1077, https://doi.org/10.1016/j.ijheatmasstransfer.2013.10.046.
[13] P.A. Libby, F.A. Williams, Strained premixed laminar flames under nonadiabatic conditions, Combust. Sci. Technol. 31 (1–2) (1983) 1–42, https://doi.org/10.1080/00102208308923629.
[14] D. Lee, S. Thakur, J. Wright, M. Ihme, W. Shyy, Characterization of flow field structure and species composition in a shear coaxial rocket GH2/GO2 injector: modeling of wall heat losses, 47th AIAA/ASME/SAE/ASEE Joint Propulsion Conference & Exhibit, AIAA Paper 2011-6125, 2011, p. 6125, , https://doi.org/10.2514/6.2011-6125.
[15] B. Fiorina, R. Baron, O. Gicquel, D. Thevenin, S. Carpentier, N. Darabiha, et al., Modelling non-adiabatic partially premixed flames using flame-prolongation of ILDM, Combust. Theor. Model. 7 (3) (2003) 449–470, https://doi.org/10.1088/1364-7830/7/3/301.
[16] D. Cecere, E. Giacomazzi, F.R. Picchia, N. Arcidiacono, F. Donato, R. Verzicco, A non-adiabatic flamelet progress–variable approach for LES of turbulent premixed flames, Flow, Turbul. Combust. 86 (3) (2011) 667–688, https://doi.org/10.1007/s10494-010-9319-7.
[17] B. Marracino, D. Lentini, Radiation modelling in non-luminous nonpremixed turbulent flames, Combust. Sci. Technol. 128 (1–6) (1997) 23–48, https://doi.org/10.1080/00102209708935703.
[18] F. Proch, A. Kempf, Modeling heat loss effects in the large Eddy simulation of a model gas turbine combustor with premixed flamelet generated manifolds, Proc. Combust. Inst. 35 (3) (2015) 3337–3345, https://doi.org/10.1016/j.proci.2014.07.036.
[19] A. Kishimoto, H. Moriai, K. Takenaka, T. Nishiie, M. Adachi, A. Ogawara, R. Kurose, Application of a nonadiabatic flamelet/progress-variable approach to large-eddy simulation of H2/O2 combustion under a pressurized condition, J. Heat Tran. 139 (12) (2017) 124501, https://doi.org/10.1115/1.4037099.
[20] S. Chan, X. Pan, M. Abou-Ellail, Flamelet structure of radiating ch4-air flames, Combust. Flame 102 (4) (1995) 438–446, https://doi.org/10.1016/0010-2180(95)00037-7.
[21] P.C. Ma, H. Wu, M. Ihme, J.-P. Hickey, Nonadiabatic flamelet formulation for predicting wall heat transfer in rocket engines, AIAA J. 56 (6) (2018) 2336–2349, https://doi.org/10.2514/1.J056539.
[22] D. Rahn, H. Riedmann, R. Behr, O.J. Haidn, Non-adiabatic flamelet modeling for the numerical simulation of methane combustion in rocket thrust chambers, 2018 Joint Propulsion Conference, 2018, p. 4869.
[23] N. Perakis, C. Roth, O.J. Haidn, Development of a non-adiabatic flamelet model for reacting flows with heat loss, Space Propulsion Conference, 2018.
[24] R. Bilger, Turbulent flows with nonpremixed reactants, in: P.A. Libby, F.A. Williams (Eds.), Turbulent Reacting Flows, Springer, Berlin, Heidelberg, 1980, pp. 65–113, , https://doi.org/10.1007/35401019269.
[25] P. Breda, M. Pfitzner, N. Perakis, O. Haidn, Generation of non-adiabatic flamelet manifolds: comparison of two approaches applied on a single-element GCH4/GO2 combustion chamber, 8th European Conference for Aeronautics and Space Sciences, EUCASS), 2019.
[26] T. Pant, C. Han, H. Wang, Computational investigations of the coupling between transient flame dynamics and thermo-acoustic instability in a self-excited resonance combustor, Combust. Theor. Model. (2019) 1–31.
[27] G. Strang, On the construction and comparison of difference schemes, SIAM J. Numer. Anal. 5 (3) (1968) 506–517, https://doi.org/10.1137/0705041.
[28] N.N. Janenko, The Method of Fractional Steps, Springer, Berlin, Heidelberg, 1971.
[29] D.G. Goodwin, H.K. Moffat, R.L. Speth, Cantera: an object-oriented software toolkit for chemical kinetics, thermodynamics, and transport processes, version 2.3.0 http://www.cantera.org retrieved 18 August 2018 (2017).
[30] N. Slavinskaya, M. Abbasi, J.-H. Starcke, A. Mirzayeva, O.J. Haidn, Skeletal mechanism of the methane oxidation for space propulsion applications, 52nd AIAA/SAE/ASEE Joint Propulsion Conference, AIAA Paper 2016-4781, 2016, p. 4781, , https://doi.org/10.2514/6.2016-4781.
[31] N. Perakis, D. Rahn, O.J. Haidn, D. Eiringhaus, Heat transfer and combustion simulation of seven-element O2/CH4 rocket combustor, J. Propul. Power 35 (6) (2019) 1080–1097.
[32] N. Perakis, C. Roth, O. Haidn, Simulation of a single-element rocket combustor using a non-adiabatic flamelet model, Space Propulsion Conference, 2018.
[33] G.K. Batchelor, Small-scale variation of convected quantities like temperature in turbulent fluid part 1. general discussion and the case of small conductivity, J. Fluid Mech. 5 (1) (1959) 113–133, https://doi.org/10.1017/S002211205900009X.
[34] U. Prüfert, F. Hunger, C. Hasse, The analysis of chemical time scales in a partial oxidation flame, Combust. Flame 161 (2) (2014) 416–426, https://doi.org/10.1016/j.combustflame.2013.09.001.

[35] R. Fox, Computational methods for turbulent reacting flows in the chemical process industry, Rev. Inst. Fr. Petrol 51 (2) (1996) 215–243.
[36] J. Caudal, B. Fiorina, M. Massot, B. Labégorre, N. Darabiha, O. Gicquel, Characteristic chemical time scales identification in reactive flows, Proc. Combust. Inst. 34 (1) (2013) 1357–1364, https://doi.org/10.1016/j.proci.2012.06.178.
[37] B.E. Launder, D.B. Spalding, Mathematical Models of Turbulence, Academic press, London-New York, 1972.
[38] M. Wolfshtein, The velocity and temperature distribution in one-dimensional flow with turbulence augmentation and pressure gradient, Int. J. Heat Mass Tran. 12 (3) (1969) 301–318, https://doi.org/10.1016/0017-9310(69)90012-X.
[39] R.B. Bird, W.E. Stewart, E.N. Lightfoot, Transport Phenomena, John Wiley & Sons, New York, 1960.
[40] C. Wilke, A viscosity equation for gas mixtures, J. Chem. Phys. 18 (4) (1950) 517–519, https://doi.org/10.1063/1.1747673.
[41] M. Ó Conaire, H.J. Curran, J.M. Simmie, W.J. Pitz, C.K. Westbrook, A comprehensive modeling study of hydrogen oxidation, Int. J. Chem. Kinet. 36 (11) (2004) 603–622.
[42] H. Negishi, Y. Daimon, H. Kawashima, N. Yamanishi, Conjugated combustion and heat transfer modeling for full-scale regeneratively cooled thrust chambers, 49th AIAA/ASME/SAE/ASEE Joint PropulsionConference, AIAA Paper 2013-3997, 2013, https://doi.org/10.2514/6.2013-3997.
[43] Y. Daimon, H. Negishi, S. Silvestri, O.J. Haidn, Conjugated combustion and heat transfer simulation for a 7 element gox/gch4 rocket combustor, 2018 Joint Propulsion Conference, AIAA Paper 2018-4553, 2018, https://doi.org/10.2514/6.2018-4553.
[44] B. Betti, D. Bianchi, F. Nasuti, E. Martelli, Chemical reaction effects on heat loads of CH4/O2 and H2/O2 rockets, AIAA J. 54 (1) (2016) 1693–1703, https://doi.org/10.2514/1.J054606.
[45] S. Silvestri, M.P. Celano, C. Kirchberger, G. Schlieben, O. Haidn, O. Knab, Investigation on recess variation of a shear coax injector for a single element GOX-GCH4 combustion chamber, transcations of the Japan society for aeronautical and space sciences, Aerospace Technology Japan 14 (ists30) (2016) 13–20, https://doi.org/10.2322/tastj.14.Pa13.
[46] N. Perakis, O.J. Haidn, Inverse heat transfer method applied to capacitively cooled rocket thrust chambers, Int. J. Heat Mass Tran. 131 (2019) 150–166, https://doi.org/10.1016/j.ijheatmasstransfer.2018.11.048.
[47] L.F. Richardson, The approximate arithmetical solution by finite differences of physical problems involving differential equations, with an application to the stresses in a masonry dam, Phil. Trans. Roy. Soc. Lond. 210 (459–470) (1911) 307–357, https://doi.org/10.1098/rsta.1911.0009.
[48] P.J. Roache, Perspective: a method for uniform reporting of grid refinement studies, J. Fluid Eng. 116 (3) (1994) 405–413, https://doi.org/10.1115/1.2910291.
[49] N. Smirnov, V. Betelin, V. Nikitin, L. Stamov, D. Altoukhov, Accumulation of errors in numerical simulations of chemically reacting gas dynamics, Acta Astronaut. 117 (2015) 338–355, https://doi.org/10.1016/j.actaastro.2015.08.013.
[50] N. Smirnov, V. Betelin, R. Shagaliev, V. Nikitin, I. Belyakov, Y.N. Deryuguin, S. Aksenov, D. Korchazhkin, Hydrogen fuel rocket engines simulation using logos code, Int. J. Hydrogen Energy 39 (20) (2014) 10748–10756, https://doi.org/10.1016/j.ijhydene.2014.04.150.